< Electronic Supporting Information>

Designing Deep Cavity Aluminum Organic Macrocycles to Trap Dyes Generating Enhanced Non-linear Optical Performance

Zhuang-Hua Liu,[a] Si-Hao Shen,[a] Cheng-Yang Zhang,[a] Jingyang Niu,[b] Qiao-Hong Li,*[a] Jian Zhang,[a] and Wei-Hui Fang*[a]

---

[a] State Key Laboratory of Structural Chemistry, Fujian Institute of Research on the Structure of Matter, Chinese Academy of Sciences, Fuzhou, Fujian 350002, China

[b] Henan Key Laboratory of Polyoxometalate Chemistry, College of Chemistry and Molecular Science, Henan University, Kaifeng, Henan 475004, PR China

Email: fwh@fjirsm.ac.cn

Content

1. Experimental Section

Chemicals and Materials

All reagents were commercially and used without further purification. Indole-2-carboxylic acid was purchased from Adamas-beta, while aluminium isopropoxide were acquired from Aladdin Chemical Reagent Shanghai. Acetonitrile (≥99.5%) were acquired from Sinopharm Chemical Reagent Beijing.

Gas Sorption Measurement

Before gas sorption, the crystals should be soaked in solvent for three days. During this time, the solvent should be exchanged several times a day. Then, the samples were degassed under a dynamic vacuum at 100 $^{\circ}$C for 10 h to obtain activated samples. The gas adsorption isotherms of active samples were obtained on a Micromeritics ASAP 2020 volumetric adsorption instrument.

Energy dispersive spectroscopy (EDS)

The EDS analyses of single crystals were performed on a JEOL JSM6700F field-emission scanning electron microscope equipped with an Oxford INCA system.

Fourier Transform Infrared (FT-IR) spectroscopies

IR spectra (KBr pellets) were recorded on an ABB Bomem MB102 spectrometer over a range 400-4000 cm^{-1}.

Thermogravimetric analyses

Thermogravimetric analysis (TGA) was performed on a Mettler Toledo TGA/SDTA 851^{e} analyzer in N_2 with a heating rate of 10 °C min^{-1} from 20 to 800 °C.

Powder X-ray diffraction (PXRD)

Powder X-ray diffraction (PXRD) data were collected on a Rigaku Mini Flex II diffractometer using CuKα radiation (λ = 1.54056 Å) under ambient conditions.

UV-vis spectroscopies

The UV-vis diffuse reflection data were recorded at room temperature using a powder sample with $BaSO_4$ as a standard (100 % reflectance) on a Perkin Elmer Lamda-950 UV spectrophotometer and scanned at 200-800 nm.

Elemental analysis

Elemental analysis (C, H and N) was carried out on a Vario Micro E III analyzer.

Contact Angle Measurements

Contact angles were tested on powder samples by using a contact angle meter with a rotatable substrate holder. 5 mg of powder samples were deposited on a glass substrate bed and flattened by glass slide. A ~20 μL water droplet was released slowly to the flat surface of the powder samples. Later, the droplet image was captured using a high-performance charge-coupled device (CCD) sensor. Five-point simulation analysis was used to analyze the contact angles of all the powder samples.

Density Functional Theory (DFT) calculation details

All the calculations were implemented in Gaussian 16.[1] The ground-state equilibrium geometries of these structures were fully optimized with density functional theory (DFT) using B3LYP functional and 6-31G(d,p) basis sets, with D3 dispersion correction of Grimme.[2-6]

Proton conductivity Measurements

The powder sample were pressed into a cylinder (0.25 cm diameter, 1.0~1.2 mm thickness) at ~0.3 MPa for 1 minutes to prevent sample decomposition from the high pressure and the thickness was measured by a vernier caliper. Then silver colloid was smeared on both sides of the pellet, which was fixed on the sample stage with gold wires. The proton conductivities of all samples were measured with Solartron SI 1260 impedance/gain-phase analyzer using a quasi-four-probe method in the frequency range of 1 to 10^6 Hz at an AC amplitude of 200 mV. The proton conductivity values were calculated with the equation $\sigma = L/RS$, where σ is the proton conductivity (S cm^{-1}), L is the thickness (cm) of the pellet, R is the bulk resistance (Ω) and S is the cross-sectional area (cm^2) of the pellet. Activation energy (Ea) for the material conductivity was estimated from the following equation: $\sigma T = \sigma_0 \exp(-Ea/k_BT)$, where σ is the proton conductivity (S cm^{-1}), σ_0 is the preexponential factor, k_B is the Boltzmann constant (eV/K), and T is the temperature (K).

Preparation of AIOCs@PDMS samples

Sylgard 184 (Dow Corning) is a kit product consisting of liquid A and B components, including basic components and a curing agent. Mixed in a weight ratio of 10:1, it is the consistency of a

medium viscosity mixed liquid. Regardless of thickness, the mixture will solidify into a transparent elastomer with toughness. PDMS samples were fabricated using Sylgard 184 (Dow Corning) by thoroughly mixing 10 parts base with 1 part curing agent.[7] The fully ground AlOCs samples were added to the PDMS mixture and stirred for three hours to form AlOCs dispersed PDMS suspension. Then the mixed suspension was added to a round mold, and then the template was placed in a vacuum oven at 60 °C for 6 h to obtain transparent and flexible AlOCs@PDMS films. The thickness of films is measured by a digital caliper (MNT951101 manufactured by Shanghai Minette).

Third-order NLO measurements

The NLO properties of the samples were evaluated using the open-aperture (OA) Z-scan technique. The excitation light source was an Nd: YAG laser with a repetition rate of 10 Hz. The laser pulses (period, 8.5 ns; wavelength, 532 nm) were split into two beams with a mirror. The pulse energies at the front and back of the samples were monitored using energy detectors D1 and D2. All of the measurements were conducted at room temperature. The samples used for NLO measurement were dispersed in DMF solution and PDMS films. Then the samples were mounted on a computer-controlled translation stage that shifted each sample along the z-axis.

$$F_{in}(z) = \frac{4\sqrt{\ln 2 E_{in}}}{\pi^{3/2}\omega(z)^2} \tag{1}$$

$$\omega(z) = \omega(0)\sqrt{1+(\frac{z}{z_0})^2} \tag{2}$$

$$T(z, s = 1) = \frac{1}{\sqrt{\pi}q_0(z,0)}\int_{-\infty}^{\infty}\ln\left[1+q_0(z,0)e^{-r^2}\right]dr \tag{3}$$

$$q_0(z,0) = \beta I_0 L_{eff} \tag{4}$$

$$L_{eff} = [1-\exp(-\alpha l)]/\alpha \tag{5}$$

$$\mathrm{Im}\,\chi^{(3)} = [\frac{10^{-7}c\lambda n^2}{96\pi^2}]\cdot\beta \tag{6}$$

$$FOM = \frac{Im\chi^{(3)}}{\beta} \tag{7}$$

In these equations, I_0 is the on-axis peak intensity at the focus (z = 0), L_{eff} is the effective thickness of the sample, l is the sample thickness, and α_0 is the linear absorption coefficient ($\alpha_0 = \ln(1/T)/d$), x = z/z_0, z is the Z-scan displacement, $\Delta\Phi$ is the phase change, ε_0 is the

permittivity of vacuum (8.85×10^{-12} F/m), c is the speed of light, n_0 is the refractive index of the medium (1.428 (DMF) or 1.403 (PDMS)). By fitting the curves, the nonlinear absorption coefficient β and the third-order non-linear susceptibilities $\chi^{(3)}$ were obtained.

2. Syntheses

Synthesis of $Al_8(L)_{16}(OH)_8 \cdot 6(H_2O) \cdot 8(MeCN)$ (AIOC-136).

A mixture of aluminium isopropoxide (0.102 g, 0.5 mmol), indole-2-carboxylic acid (0.161 g, 1.0 mmol) and acetonitrile (5 mL) was sealed in a 20 mL vial and transferred to a preheated oven at 100 ^{o}C for 3 days. When cooled to room temperature, colourless crystals were obtained. (yield: ~110mg, ~59 % based on $Al(O^iPr)_3$). The crystals are rinsed with acetonitrile and preserved under a sealed and dry environment. FT-IR (KBr, cm^{-1}): 3605(w), 3453(w), 1538(s), 1430(s), 1332(s), 784(s), 747(m), 594(s). Elemental analysis calcd. (%) for $C_{158}H_{137}Al_8N_{23}O_{46}$ (MW 3309.74): C 57.28, N 9.72, H 4.13; found C 56.98, N 9.40, H 4.12.

Scale-up synthesis of AIOC-136.

A mixture of aluminium isopropoxide (1.020 g), indole-2-carboxylic acid (1.610 g), and acetonitrile (50 mL) was sealed in a 100 mL vial and heated at 100 °C for 3 days. When cooled to room temperature, colorless crystals were obtained. (yield: ~700mg, ~38% based on $Al(O^iPr)_3$).

Synthesis of $Al_8(L)_{16}(OH)_8 \cdot 2(HAO7) \cdot 2(H_2O) \cdot 2(MeCN) \cdot n(solvent)$ (AIOC-136-HAO7).

A mixture of aluminium isopropoxide (0.102 g, 0.5 mmol), indole-2-carboxylic acid (0.161 g, 1.0 mmol), acid orange 7 (0.087 g, 0.24 mmol) and acetonitrile (5 mL) was sealed in a 20 mL vial and heated at 100 ^{o}C for 3 days. When cooled to room temperature, red crystals were obtained after rinsed with acetonitrile and preserved under a sealed and dry environment. (yield: ~78mg, ~34 % based on $Al(O^iPr)_3$). FT-IR (KBr, cm^{-1}): 3596(w), 3285(w), 1538(s), 1435(s), 1338(s), 1031(m), 747(s), 597(s). Elemental analysis calcd. (%) for $C_{180}H_{138}Al_8N_{22}O_{50}S_2$ (MW 3689.08): C 48.59, N 8.34, H 4.07; found C 48.83, N 8.05, H 4.11.

X-ray Crystallographic Analyses

Crystallographic data of crystal **AIOC-136** and **AIOC-136-HAO7** were collected on Hybrid Pixel Array detector equipped with Ga-Kα radiation (λ = 1.3405 Å) at about 100 K. The structures were solved with the dual-direct methods using ShelxT and refined with the full-matrix least-squares technique based on F^2 using the *SHELXL*-2014.[8] Non-hydrogen atoms were refined anisotropically. Hydrogen atoms were added theoretically, riding on the concerned atoms and refined with fixed thermal factors. Solvent molecules in the lattice could not be modeled in terms of atomic sites and were treated using the SQUEEZE routine in the PLATON software package,[9] whose amounts were determined by TGA. The number of solvent molecules removed has been added to the cif file (**AIOC-136**). The naphthol ring on HAO7 has a statistical phenomenon which occupy 0.5, respectively (**AIOC-136-HAO7**). Some water guests are severely disordered, thus, the related hydrogen atoms could not be added (**AIOC-136-HAO7**). All absorption corrections were performed using the multi-scan program. The obtained crystallographic data for these molecular rings are summarized in Table S1.
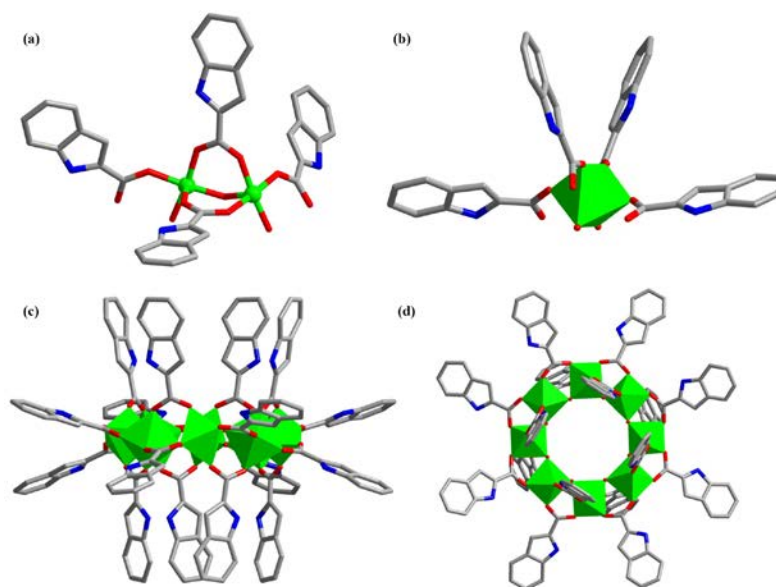
3. Structure description

Figure S1. (a) The smallest asymmetric unit of **AIOC-136**. (b) Coordination environment and octahedral structure of Al(Ⅲ) ion in **AIOC-136**. (c) Side view of **AIOC-136**. (d) Top view of **AIOC-136**. Hydrogen atoms are omitted for clarity. Color codes: green Al, red O, blue N and gray C.
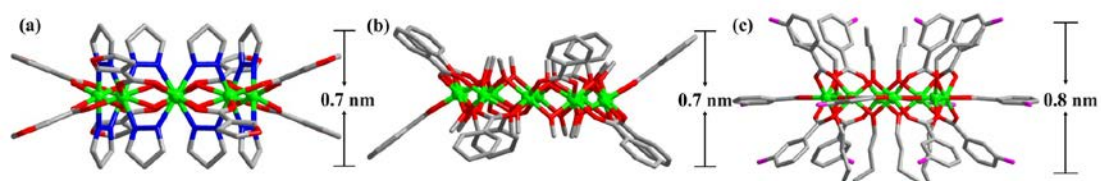
Figure S2. (a) The depth of **AlOC-21**. (b) The depth of **AlOC-3**. (c) The depth of **AlOC-1**. Hydrogen atoms are omitted for clarity. Color codes: green Al, red O, blue N, pink F and gray C.
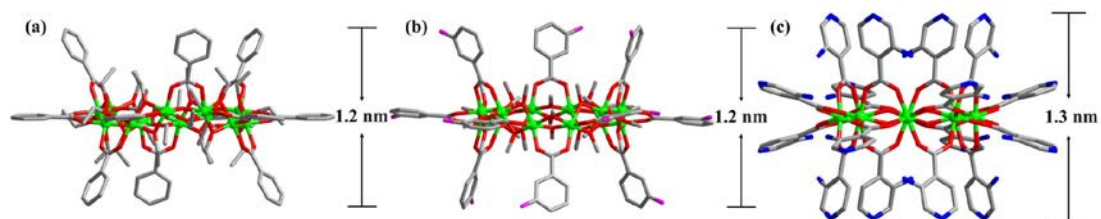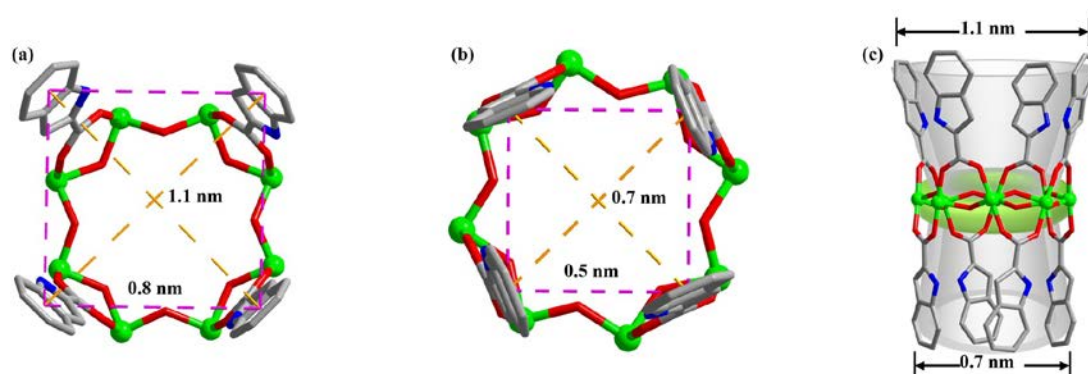

Figure S3. (a) The depth of **AlOC-6**. (b) The depth of **AlOC-7**. (c) The depth of **AlOC-59**. Hydrogen atoms are omitted for clarity. Color codes: green Al, red O, blue N, pink F and gray C.

Figure S4. The upper-rim lengths (a), the lower-rim lengths (b) and the side view (right) of **AlOC-136**. The ligands at equatorial position and hydrogen atoms are omitted for clarity. Color codes: green Al, red O, blue N and gray C.
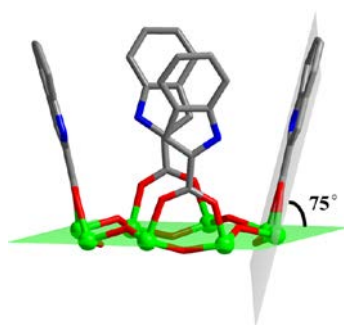
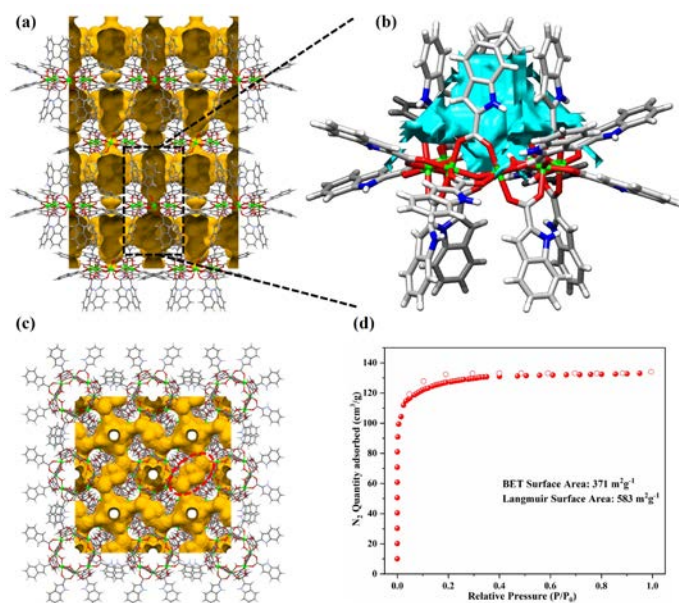Figure S5. The dihedral angles between the ligand at β position and aluminum inorganic ring plane.

Figure S6. (a) Packing in **AIOC-136** along [0 1 0] direction. The 1D intramolecular deep cavity has been highlighted by the black square frame. (b) The surface and deep cavity of **AIOC-136** were calculated via the 3V Volume Assessor program.[10] The calculated surface area is 846 Å^2, and the calculated volume is 202 Å^3. (c) Packing in **AIOC-136** along [0 0 1] direction. The intermolecular pore has been highlighted by the red circle. (d) N$_2$ adsorption isotherms for **AIOC-136** at 77 K. Color codes: green Al, red O, blue N, white H and gray C.
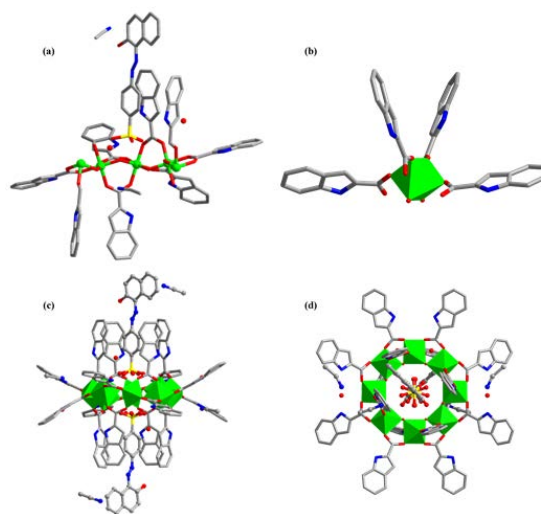

Figure S7. (a) The smallest asymmetric unit of **AIOC-136-HAO7**. (b) Coordination environment and octahedral structure of Al(Ⅲ) ion in **AIOC-136-HAO7**. (c) Side view of **AIOC-136-HAO7**. (d) Top view of **AIOC-136-HAO7**. Hydrogen atoms are omitted for clarity. Color codes: green Al, red O, blue N, yellow S and gray C.
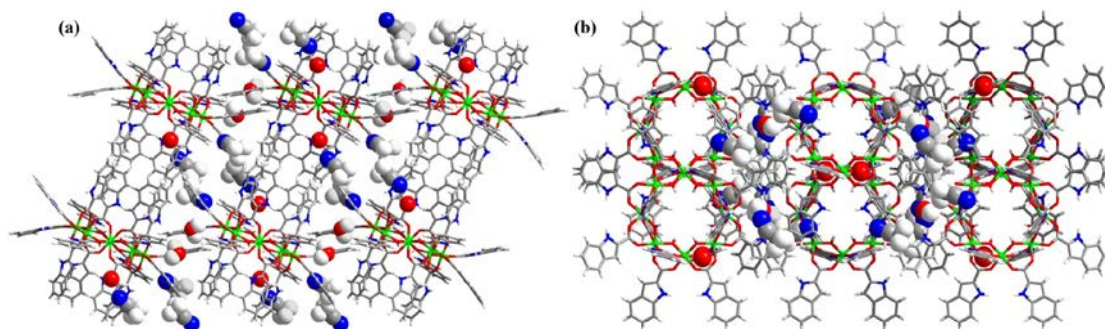
Figure S8. Solvent guests interact adhesive in the intermolecular voids with hydrophobicity. (a) Packing in **AIOC-136-HAO7** along [0 1 0] direction. (b) Packing in **AIOC-136-HAO7** along [0 0 1] direction. The HAO7 dye molecules are omitted for clarity. Color codes: green Al, red O, blue N and gray C.
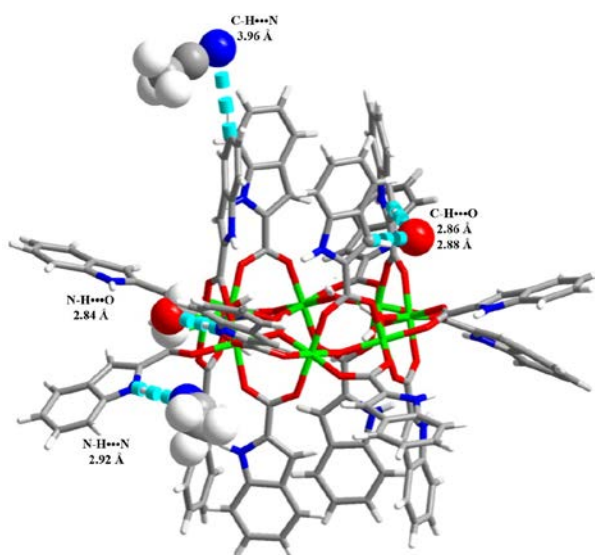

Figure S9. The hydrogen bond interactions between solvent molecules and host. The HAO7 dye molecules are omitted for clarity. Color codes: green Al, red O, blue N and gray C.
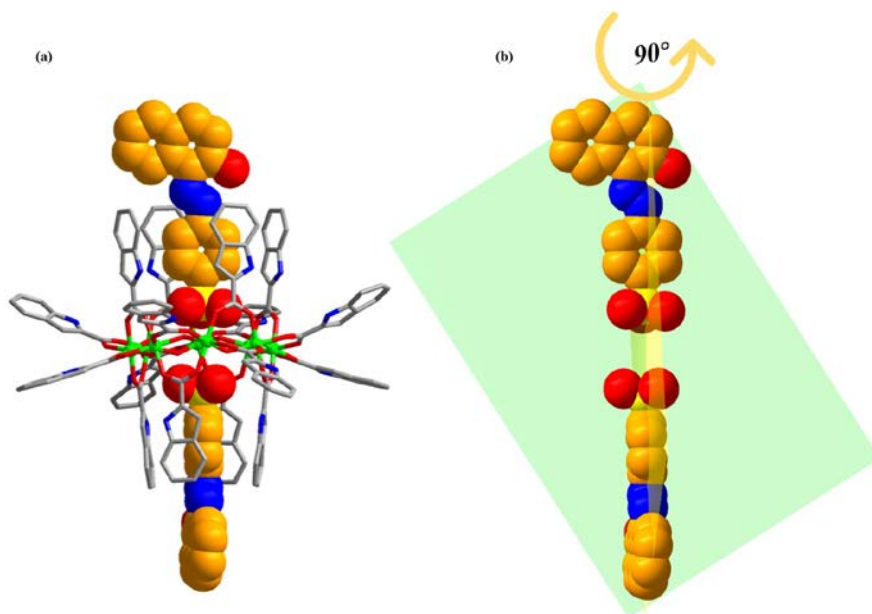
Figure S10. (a) Side view of the large ring capturing two HAO7 molecules. (b) The torsion angle between two HAO7 molecules. Hydrogen atoms are omitted for clarity. Color codes: green Al, red O, blue N, yellow S, gray C from host and orange C from guest.
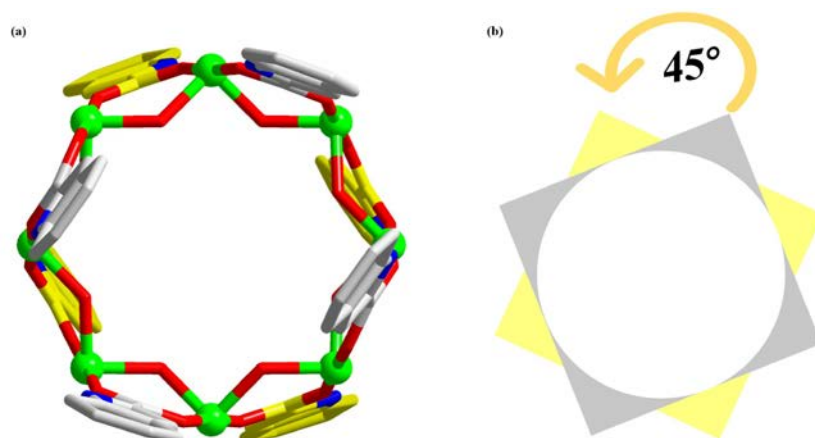

Figure S11. (a) Top view of the large ring. (b) The torsion angle between the upper (gray) and lower (yellow) ligands of the cavity. Hydrogen atoms are omitted for clarity. Color codes: green Al, red O and blue N.
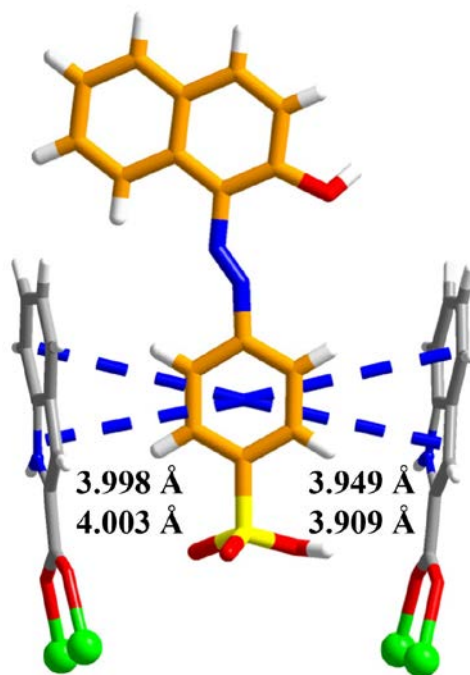
Figure S12. T-shape configuration π-π interactions between host and guest. Color codes: green Al, red O, blue N, yellow S, gray C from host and orange C from guest.
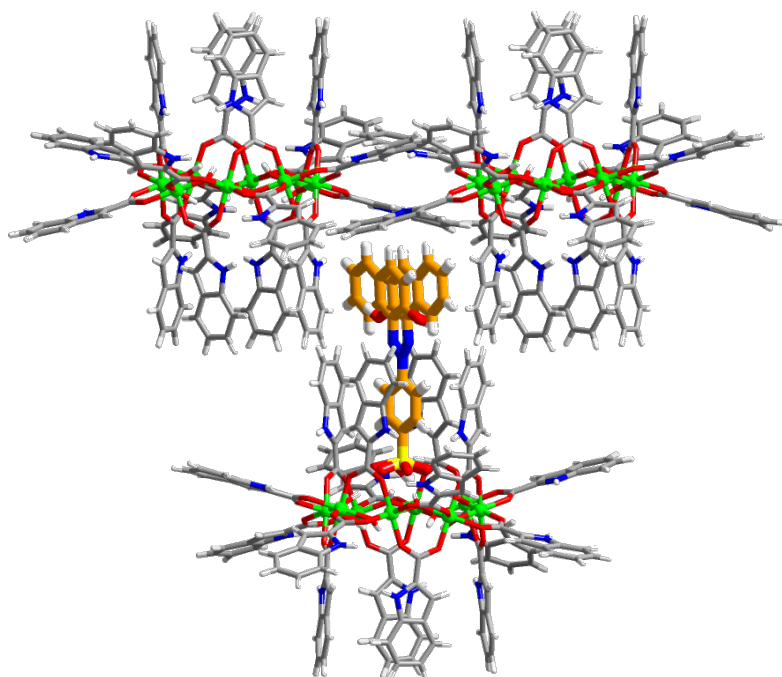

Figure S13. The positional relationship between the naphthol ring on HAO7 and the adjacent aluminum ring. Color codes: green Al, red O, blue N, yellow S, gray C from host and orange C from guest.
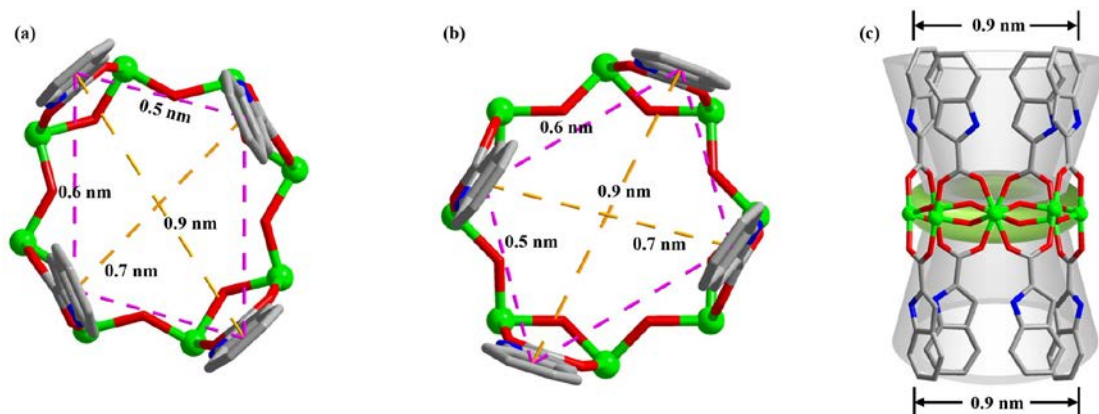
Figure S14. The upper-rim lengths (a), the lower-rim lengths (b) and the side view (c) of **AIOC-136-HAO7**. The ligands at equatorial position and hydrogen atoms are omitted for clarity. Color codes: green Al, red O, blue N and gray C.
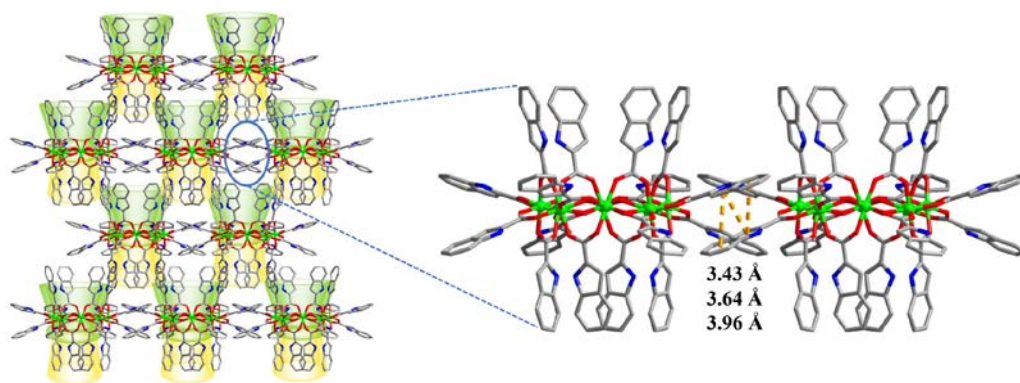

Figure S15. The -AB- alternating supramolecular stacking and the intermolecular π···π stacking interactions in **AIOC-136**. Hydrogen atoms are omitted for clarity. Color codes: green Al, red O, blue N and gray C.
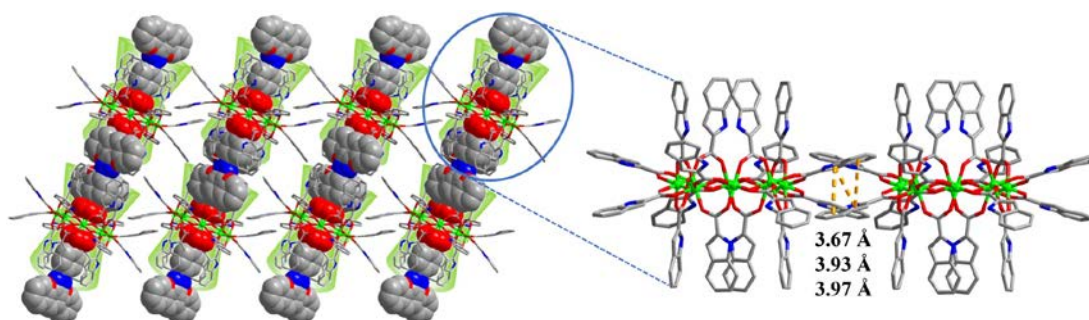

Figure S16. The -AA- alternating supramolecular stacking and the intermolecular π···π stacking interactions in **AIOC-136-HAO7**. Hydrogen atoms are omitted for clarity. Color codes: green Al, red O, blue N, yellow S and gray C.
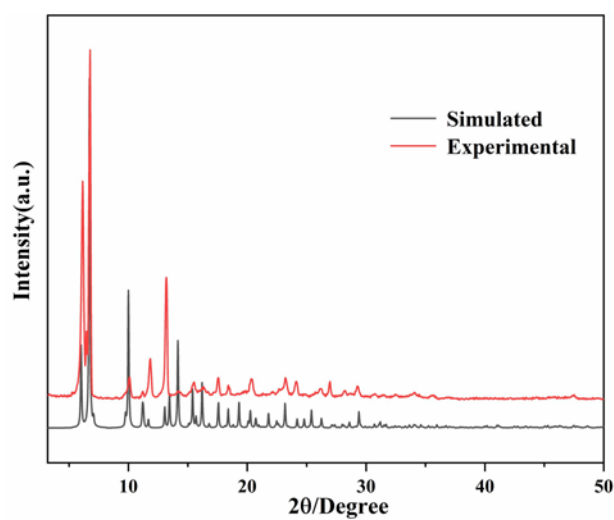
4. PXRD for AIOC-136 and AIOC-136-HAO7

Figure S17. The PXRD of the simulated and experimental patterns of **AlOC-136**.
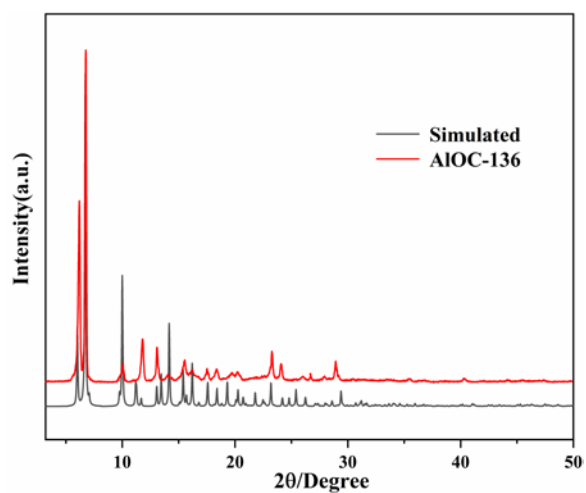
Figure S18. The PXRD of the simulated and experimental patterns of **AlOC-136** after soaking in the water for 12h.

Figure S19. The PXRD of the simulated and experimental patterns of **AlOC-136-HAO7**.

5. Stability studies for AlOC-136 and AlOC-136-HAO7

Figure S20. X-ray single crystal diffraction points of **AIOC-136** after soaking in the aqueous solution over a pH range of 2-7 for 48 h.
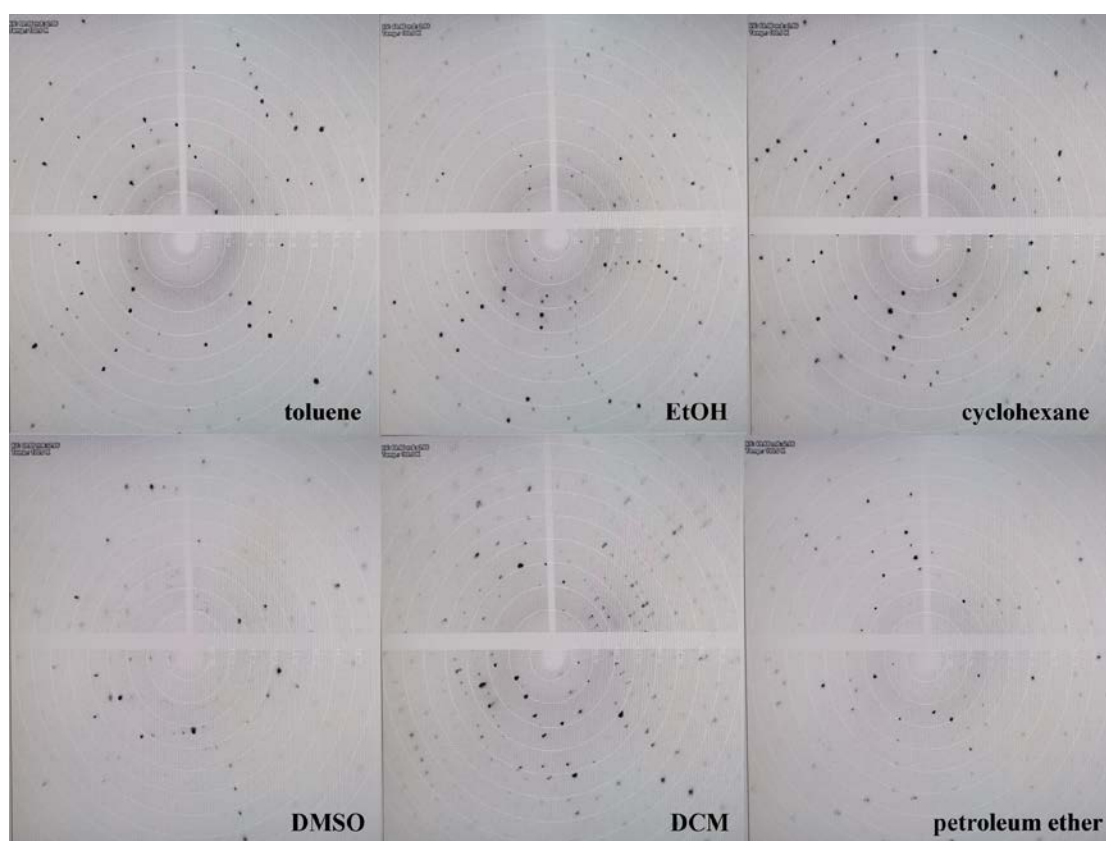
Figure S21. X-ray single crystal diffraction points of **AIOC-136** after soaking in different organic solvents for 48 h.

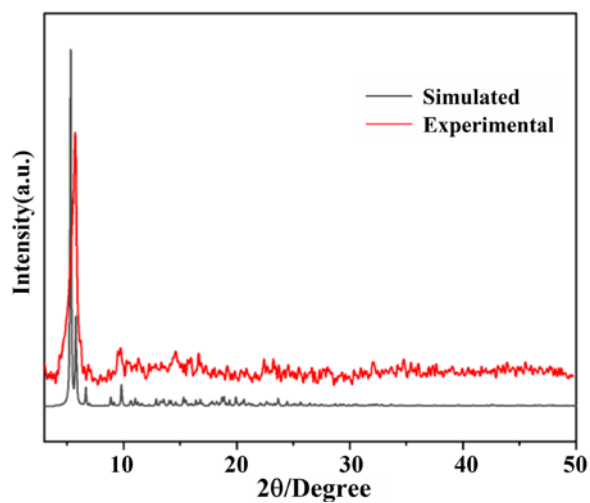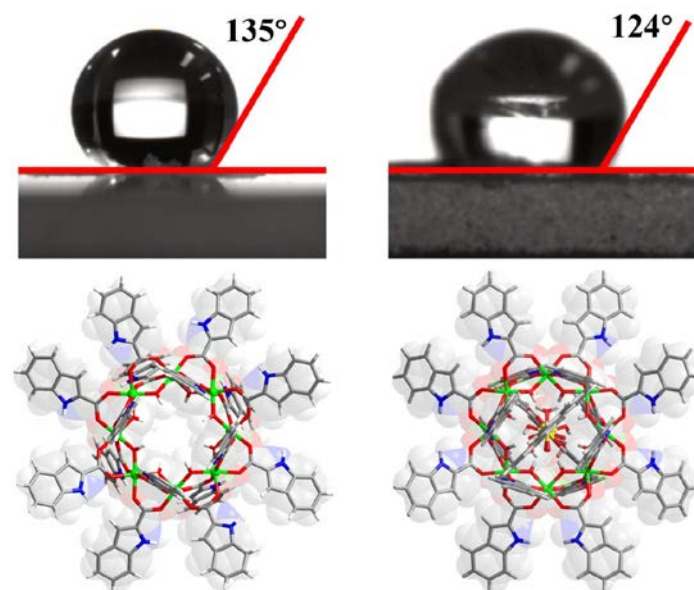Figure S22. Tunable wettability of the molecular rings. Experimentally measured contact angles of the water droplet on **AIOC-136** (left), **AIOC-136-HAO7** (right) surface and the structures of the corresponding compounds. Space-filling view is used to emphasize the organic shell of the molecular rings.

6. Studies of dye molecule adsorption for AIOC-136
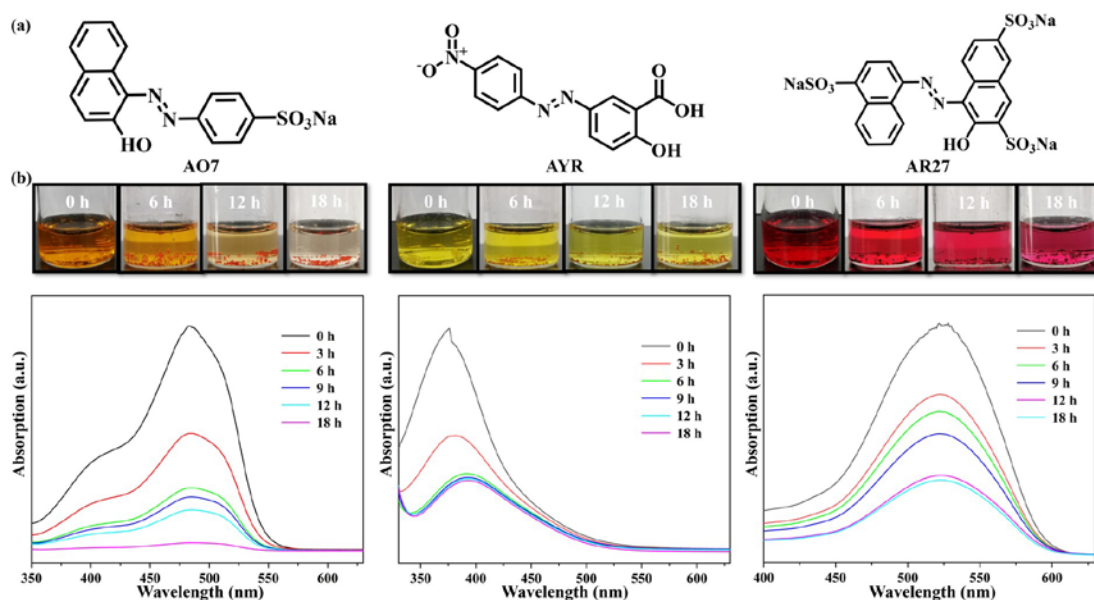
Figure S23. (a) Structures of NaAO7, AYR and AR27 dyes. (b) Photos of dye absorption by **AIOC-136** and absorption peak of dye at different time intervals. Initial conc. of dyes: 0.14×10^{-3} M; adsorbent dose: 10 mg.
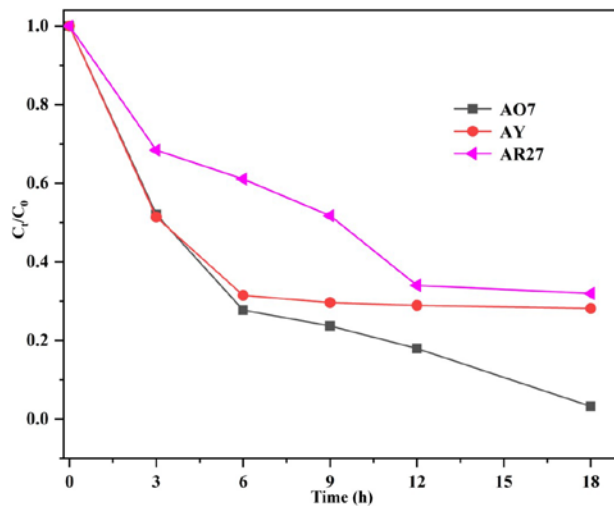
Figure S24. Adsorption rate of different dyes solutions with **AIOC-136** (C_0 is the initial concentration of the dyes and C_t is the concentration of the dyes at any given time). Initial conc. of dyes: 0.14×10^{-3} M; adsorbent dose: 10 mg.

7. Hirshfeld surface analysis for AlOC-136-HAO7
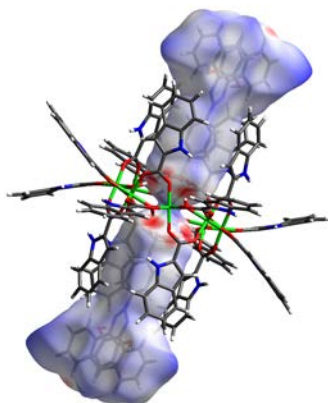
Figure S25. Hirshfeld surface analysis mapped over d_{norm} for **AlOC-136-HAO7**. In the color scale, negative values of d_{norm} are distinguished by contacts in red that are smaller than the van der Garde sum Walls radius. While the blue area corresponds to longer contacts with positive d_{norm} values, the white area indicates intermolecular distances close to van der Waals contacts with zero d_{norm} values.

$$d_{norm} = \frac{d_i - ri^{vdw}}{r_i^{vdw}} + \frac{d_e - re^{vdw}}{r_e^{vdw}}$$

d_e is the distance to the nearest atom external to the surface, d_i is the distance to the nearest atom internal to the surface. Both '*de*' and '*di*' and the vdW radii of the atom which are utile for the normalized contact distance (d_{norm}) enables identification of the regions of particular importance to intermolecular interactions.

Figure S26. Fingerprint plots of major contacts in **AIOC-136-HAO7**.

8. FT-IR spectra for AIOC-136 and AIOC-136-HAO7

Figure S27. FT-IR spectrum for **AIOC-136**.
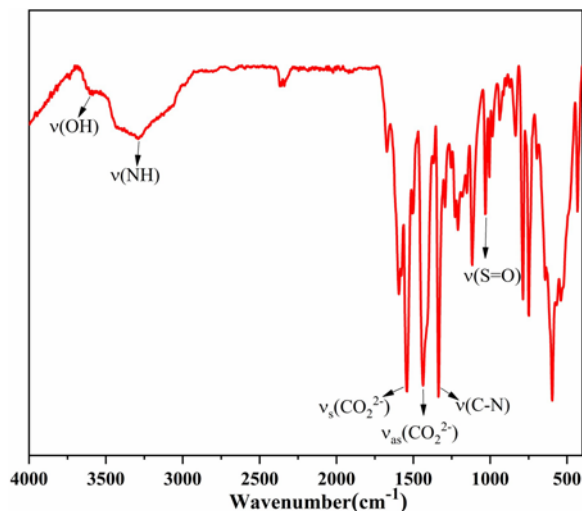
Figure S28. FT-IR spectrum for **AIOC-136-HAO7**.

Discussion for IR spectra:

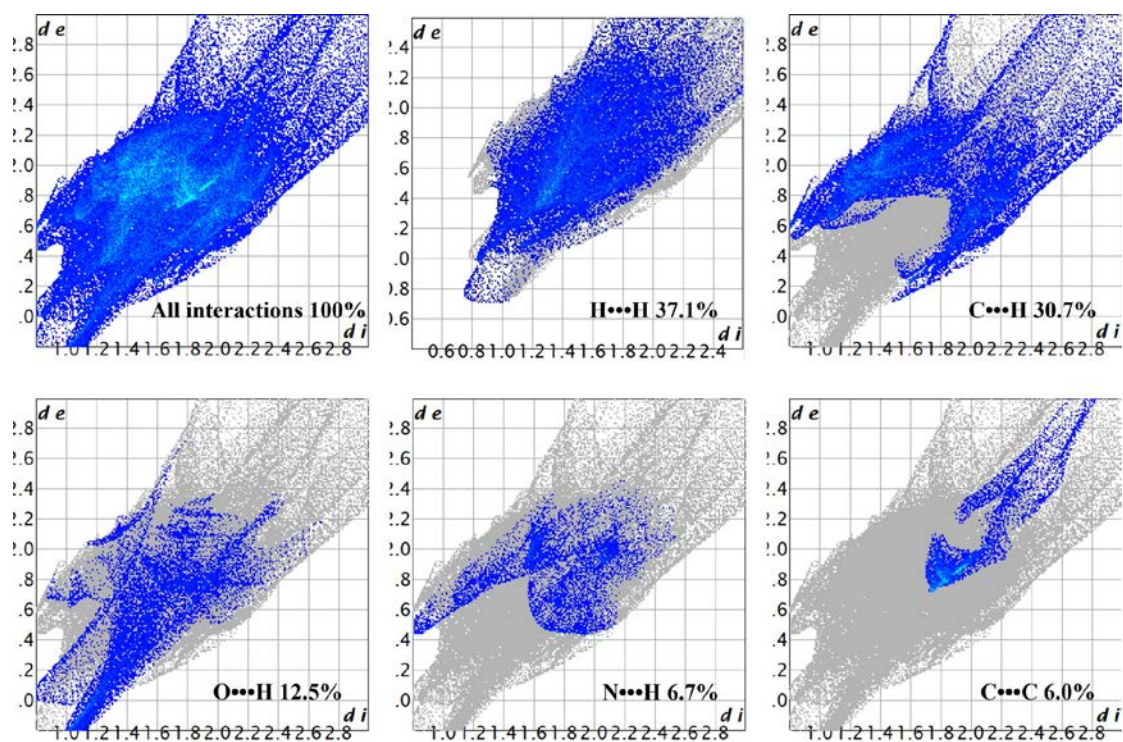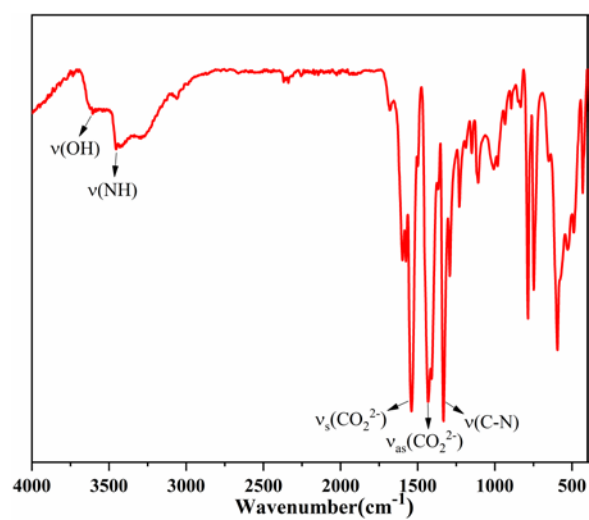FT-IR spectra have been recorded on solid samples palletized with KBr, which are presented in Supplementary Figures 27–28. In the high wavenumber region ($v > 1000$ cm^{-1}), the weak absorption bands at 3605−3596 cm^{-1} and 3453−3285 cm^{-1} can be ascribed to the stretching vibrational modes of O-H bonds in hydroxyl groups and N-H in indole units, respectively. The characteristic stretching vibrations $v(CO_2^{2-})$ of in carboxylic groups is overlapped from 1538 cm^{-1} to 1430 cm^{-1}. Among them, the asymmetric stretching vibration (v_{as}) and symmetric stretching vibration (v_s) of the carboxylate group can be attributed, namely, the band at 1538 cm^{-1} is assigned to the $v_{as}(CO_2^{2-})$ whilst the signal at 1430 cm^{-1} is ascribed to the $v_s(CO_2^{2-})$. The strong absorption bands at 1332−1338 cm^{-1} can be ascribed to the stretching vibrational modes of C-N bonds in indole units. In compound **AIOC-136-HAO7**, the stretching vibrations (v) for -SO$_3$H from HAO7 guests appeared at 1031 cm^{-1}.[11]

9. TGA curves for AIOC-136 and AIOC-136-HAO7
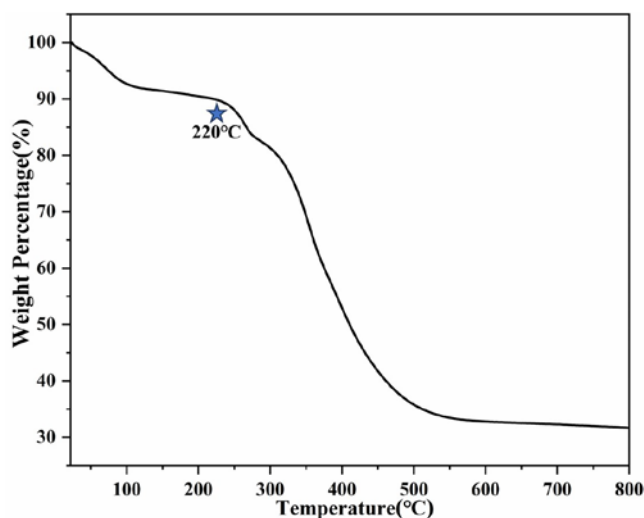
Figure S29. TGA curve of **AIOC-136**.
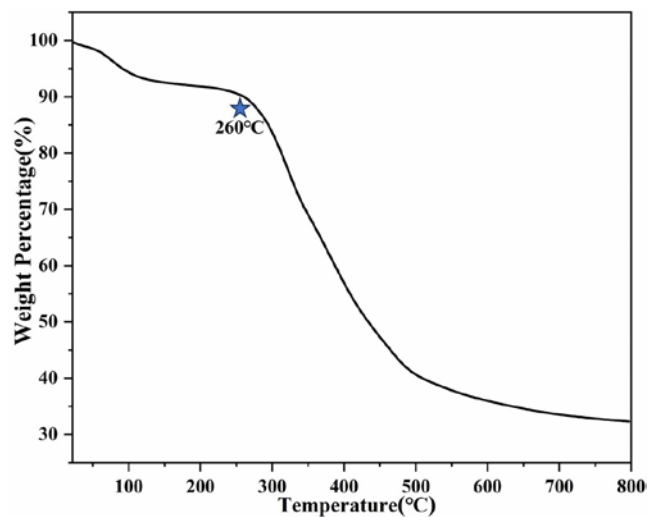
Figure S30. TGA curve of **AlOC-136-HAO7**.

Discussion for TGA curves:

TGA curves show that **AlOC-136** decompose at about 220°C while **AlOC-136-HAO7** can maintain structural stability at about 260°C. The first weight loss of 8.59% for **AlOC-136** and 7.86% for **AlOC-136-HAO7** is corresponded to the release of solvent guest molecules such as water and acetonitrile. The severe weight loss after 220°C or 260°C indicates the skeleton collapse of Al$_8$ ring.

10. TGA curves for AIOC-136 and AIOC-136-HAO7
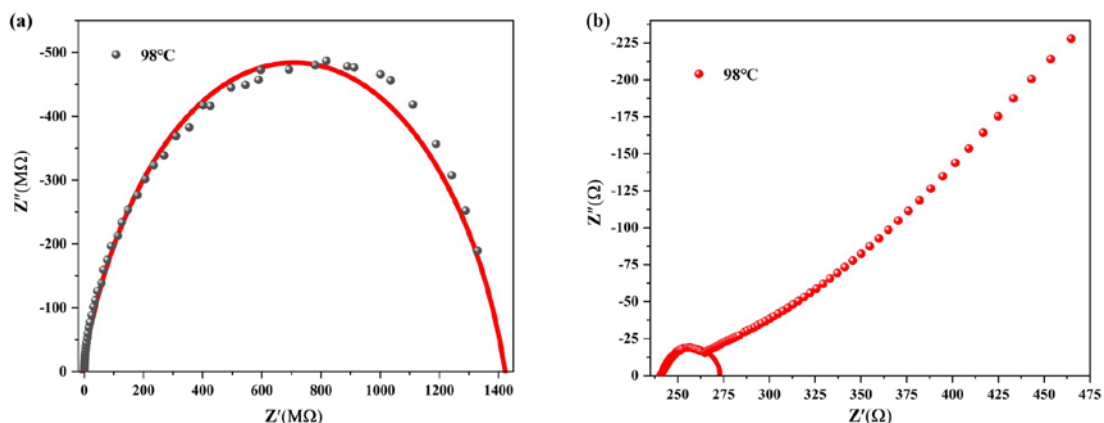
Figure S31. Nyquist plots of **AIOC-136** (a) and **AIOC-136-HAO7** (b) at 98°C and 98% RH.
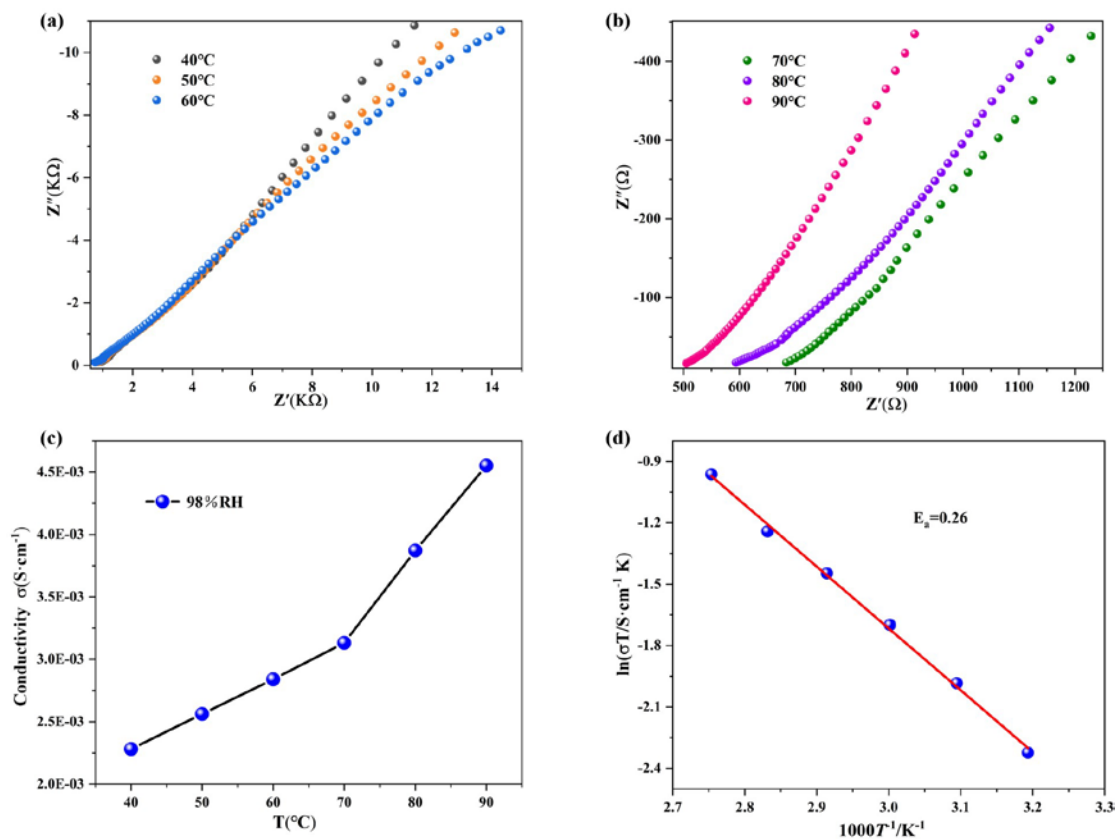
Figure S32. (a, b) Nyquist plots of **AIOC-136-HAO7** from 40 to 90°C at 98% RH. (c) The proton conductivity of **AIOC-136-HAO7** from 40 to 90°C at 98% RH. (d) Temperature-dependent conductivities of **AIOC-136-HAO7**.

11. Third-order NLO measurements
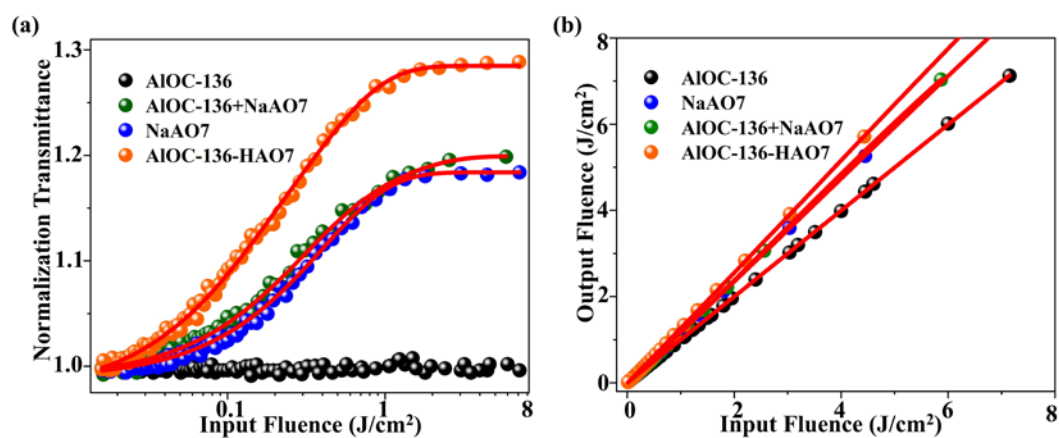
Figure S33. (a) The OL curves, (b) the curves of output fluence versus input fluence of samples dispersing in DMF solution at 532 nm (input energy: 100 uJ).
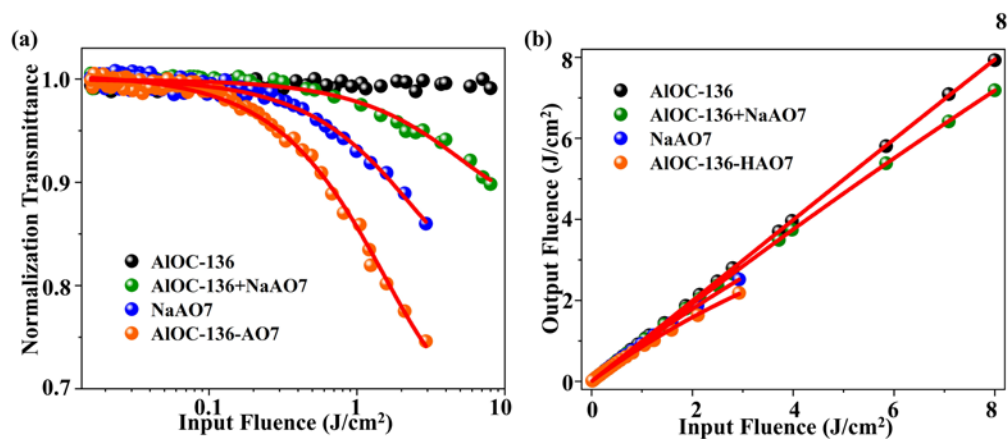
Figure S34. The OL curves, (b) the curves of output fluence versus input fluence of samples dispersing in PDMS films at 532 nm (input energy: 100 uJ).

12. Summary of crystallography data for AIOC-136, AIOC-136-HAO7 and AIOC-136'.

Table S1. Crystallographic data and structure refinement parameters of **AIOC-136**, **AIOC-136-HAO7** and **AIOC-136'.**

|	AIOC-136	AIOC-136-HAO7	AIOC-136'
CCDC Nos.	2304752	2304753	
Empirical formula	$C_{158}H_{139}Al_8N_{23}O_{47}$	$C_{180}H_{138}Al_8N_{22}O_{50}S_2$	$C_{148}Al_8N_{18}O_{40}$
Formula weight	3327.75	3689.08	2885.50
Temperature / K	100.00(3)	100.00(10)	100.0(4)
Crystal system	tetragonal	monoclinic	Tetragonal
Space group	$P4nc$	$C2/c$	$P4/nnc$
a [Å]	17.7456(10)	36.0720(4)	17.7876(2)
b [Å]	17.7456(10)	17.8247(10)	17.7876(2)
c [Å]	26.2982(3)	36.3988(4)	26.6956(5)
α [°]	90	90	90
β [°]	90	113.08(10)	90
γ [°]	90	90	90
V [Å³]	8281.47(13)	21530.2(4)	8446.5(2)
Z	2	4	2
ρcalc [g cm⁻³]	1.335	1.138	1.135
μ [mm⁻¹]	0.779	0.752	0.704
F (000)	3456.0	7632.0	2876.0
Index ranges	$-21 \leq h \leq 22$	$-46 \leq h \leq 46$	$-22 \leq h \leq 22$
	$-22 \leq k \leq 22$	$-11 \leq k \leq 23$	$-22 \leq k \leq 22$
	$-34 \leq l \leq 33$	$-47 \leq l \leq 44$	$-343 \leq l \leq 33$
Reflections collected	163455	78783	160439
Independent refs [R_{int}]	9340 [0.0475]	23542 [0.0634]	4324[0.0539]
data/restraints/parameters	9340/14/469	23542/13/1306	4324/127/233
Goodness-of-fit on F^2	1.065	1.785	3.417
R_1, wR_2 [I > 2σ(I)]	0.0523, 0.1491	0.1367, 0.3845	0.2066, 0.6201
R_1, wR_2 [all data]	0.0568, 0.1535	0.1568, 0.4002	0.2122, 0.6288

13. The summary of cavity size from classic pure organic macrocycles

Table S2. Comparison with other reported classic pure organic macrocycles.

	Cavity Depth (Å)	Cavity diameter (Å)
[18]crown-6[12]	1.7	4.0
α-cyclodextrins[13]	4.8	5.0
calix[4]A[14]	4.9	2.0
cucurbit[6]uril[15]	5.9	5.8
pillar[5]arene[13,16]	7.7	5.0
corral[5]arene[16]	12.7	6.2
AIOC-136	17.9	5.0

14. The hydrogen bonding parameters for AIOC-136-HAO7

Table S3. Hydrogen bonding parameters between solvent molecules and host.

	Distance(Å)		Angle (°)	
Bond	H···A	D···A	D-H···A	Symmetry
N01I-H01I···O1AA	1.97	2.848(10)	172	x, y, z
C00S-H00S···O1	2.00	2.865(13)	150	1-x, y, 3/2-z
C00W-H00W···O1	1.94	2.881(11)	171	1-x, y, 3/2-z
N01A-H01A···N1AA	2.05	2.93(2)	174	x, y, z
C02L-H02L···N1	3.20	3.964(19)	138	x, y, z

Table S4. Hydrogen bonding parameters between HAO7 molecule and host.

	Distance(Å)		Angle (°)	
Bond	H···A	D···A	D-H···A	Symmetry
O007-H007···O24	1.84	2.691(14)	162	x, y, z
O007-H007···O036	1.87	2.699(15)	156'	x, y, z
O08-H08···O025	1.86	2.728(8)	166	x, 1-y, -1/2+z
O09-H09···O039	1.87	2.736(8)	170	x, y, z

| O00C-H00C···O4 | 1.94 | 2.777(17) | 159 | x, 1-y, -1/2+z |
| O00C-H00C···O4 | 1.87 | 2.704(17) | 157' | x, 1-y, -1/2+z |

15. The summary of non-linear optical parameters

Table S5. Linear transmittance (T%), linear absorption coefficient (α), non-linear absorption coefficient (β), imaginary part of third-order non-linear susceptibility ($\chi^{(3)}$), FOM and maximum non-linear transmittances T_{max} of the **AIOC-136-HAO7**, NaAO7 and **AIOC-136**+NaAO7 dispersing in DMF solution.

Samples	T(%)	α(cm^{-1})	β(cm/GW)	Im$\chi^{(3)}$(×10^{-12}esu)	*FOM*(×10^{-12}esu)	T_{max}
AIOC-136-HAO7	52	6.54	-15.98	-3.50	0.53	1.28
NaAO7	52	6.54	-11.56	-2.53	0.38	1.18
AIOC-136+NaAO7	52	6.54	-11.58	-2.54	0.39	1.19

Table S6. Linear transmittance (T%), linear absorption coefficient (α), non-linear absorption coefficient (β), imaginary part of third-order non-linear susceptibility ($\chi^{(3)}$), *FOM* and minimum non-linear transmittances T_{min} of the **AIOC-136-HAO7**, NaAO7 and **AIOC-136**+NaAO7 dispersing in PDMS films.

Samples	T(%)	α(cm^{-1})	β(cm/GW)	Im$\chi^{(3)}$(×10^{-12}esu)	*FOM*(×10^{-12}esu)	T_{max}
AIOC-136-HAO7	58	5.44	32.15	6.80	1.25	0.73
NaAO7	58	5.44	11.57	1.74	0.32	0.87
AIOC-136+NaAO7	58	5.44	11.54	1.73	0.31	0.89

16. References

[1] M. J. Frisch, G. W. Trucks, H. B. Schlegel, G. E. Scuseria, M. A. Robb, J. R. Cheeseman, G. Scalmani, V. Barone, G. A. Petersson, H. Nakatsuji, X. Li, M. Caricato, A. V. Marenich, J. Bloino, B. G. Janesko, R. Gomperts, B. Mennucci, H. P. Hratchian, J. V. Ortiz, A. F. Izmaylov, J. L. Sonnenberg, D. Williams-Young, F. Ding, F. Lipparini, F. Egidi, J. Goings, B. Peng, A. Petrone, T. Henderson, D. Ranasinghe, V. G. Zakrzewski, J. Gao, N. Rega, G. Zheng, W. Liang, M. Hada, M. Ehara, K. Toyota, R. Fukuda, J. Hasegawa, M. Ishida, T. Nakajima, Y. Honda, O. Kitao, H. Nakai, T. Vreven, K. Throssell, J. A. Montgomery, Jr., J. E. Peralta, F. Ogliaro, M. J. Bearpark, J. J. Heyd, E. N. Brothers, K. N. Kudin, V. N. Staroverov, T. A. Keith, R. Kobayashi, J. Normand, K. Raghavachari, A. P. Rendell, J. C. Burant, S. S. Iyengar, J. Tomasi, M. Cossi, J. M. Millam, M. Klene, C. Adamo, R.

Cammi, J. W. Ochterski, R. L. Martin, K. Morokuma, O. Farkas, J. B. Foresman, D. J. Fox, Gaussian 16, revision C. 01, Gaussian, Inc.: Wallingford CT, 2016.

[2]   A. D. Becke, *Phys. Rev. A* 1988, **38**, 3098-3100.

[3]   C. Lee, W. Yang, R. G. Parr, *Phys. Rev. B* 1988, **37**, 785-789.

[4]   A. D. Becke, *J. Chem. Phys.* 1993, **98**, 1372-1377.

[5]   P. J. Stephens, F. J. Devlin, C. F. Chabalowski, M. J. Frisch, *J. Phys. Chem.* 1994, **98**, 11623-11627.

[6]   S. Grimme, J. Antony, S. Ehrlich, H. Krieg, *J. Chem. Phys.* 2010, **132**, 154104.

[7]   D.-J. Li, Q.-h. Li, Z.-R. Wang, Z.-Z. Ma, Z.-G. Gu, J. Zhang, *J. Am. Chem. Soc.* 2021, **143**, 17162-17169.

[8] G. M. Sheldrick, SHELXL-2014 Program for Crystal Structure Solution and Refinment, (Univerity of Göttingen, Germany, 2014).

[9] A. L. Spek, *Acta Crystallogr. Sect. C Struct. Chem.* 2015, **71**, 9-18.

[10] N. R. Voss, M. Gerstein, *Nucleic Acids Res.* 2010, **38**, W555-W562.

[11] B. Shi, X. Pang, S. Li, H. Wu, J. Shen, X. Wang, C. Fan, L. Cao, T. Zhu, M. Qiu, Z. Yin, Y. Kong, Y. Liu, M. Zhang, Y. Liu, F. Pan, Z. Jiang, *Nat. Commun.* 2022, **13**, 6666.

[12] C. J. Pedersen, *J. Am. Chem. Soc.* 1967, **89**, 2495-2496.

[13] T. Ogoshi, S. Kanai, S. Fujinami, T.-a. Yamagishi, Y. Nakamoto, *J. Am. Chem. Soc.* 2008, **130**, 5022-5023.

[14] C. D. Gutsche, *Acc. Chem. Res.* 1983, **16**, 161.

[15] K.-M. Park, D. Whang, E. Lee, J. Heo, K. Kim, Chem. Eur. J. 2002, **8**, 498-508.

[16] H. Han, R. Fu, R. Wang, C. Tang, M.-M. He, J.-Y. Deng, D.-S. Guo, J. F. Stoddart, K. Cai, *J. Am. Chem. Soc.* 2022, **144**, 20351-20362.